Estimation of Dielectric Parameters from Ultrasound Waves in Quantitative Thermoacoustic Tomography

Teemu Sahlström 1 and Tanja Tarvainen 1

¹Department of Technical Physics, University of Eastern Finland, Kuopio, Finland

Abstract

Thermoacoustic tomography (TAT) is an imaging modality based on the thermoacoustic effect. In TAT, a short microwave or radio wave pulse is directed to the imaged target. The energy of the electromagnetic pulse is absorbed depending on the target's dielectric parameters, resulting in a spatially varying pressure distribution via the thermoacoustic effect. This pressure, known as the initial pressure distribution, relaxes as broadband ultrasound waves that are measured on the boundary of the target. In the inverse problem of TAT, the initial pressure is estimated from the measured ultrasound waves. TAT can further be extended to quantitative TAT (QTAT), where the aim is to estimate the dielectric parameters of the imaged target by utilizing a model for electromagnetic wave propagation. In this work, we consider the QTAT problem and propose an approach for simultaneous estimation of electrical conductivity and permittivity from the ultrasound waves. The problem is approached in the framework of Bayesian inverse problems. The forward model describing electromagnetic and acoustic wave propagation is based on Maxwell's equations and the acoustic wave equation, respectively. The approach is evaluated with numerical simulations. The results show that the dielectric parameters can be accurately estimated using the proposed approach. However, the ultrasound sensor geometry and the number of electromagnetic pulses have a significant effect on the accuracy of the estimated parameters.

This work was supported by the European Research Council (ERC) under the European Union's Horizon 2020 Research and Innovation Program (Grant Agreement No. 101001417-QUANTOM) and the Research Council of Finland (Centre of Excellence in Inverse Modelling and Imaging grant 353086, and Flagship of Advanced Mathematics for Sensing Imaging and Modelling grant 358944). The authors wish to acknowledge CSC – IT Center for Science, Finland, for computational resources. This work has been submitted to the IEEE for possible publication. Copyright may be transferred without notice, after which this version may no longer be accessible.

1 Introduction

Thermoacoustic tomography (TAT) is a biomedical imaging modality based on the thermoacoustic effect [1–8]. In TAT, a short microwave or radio wave pulse is directed to the imaged target. As the electromagnetic waves propagate through the target, they are absorbed, leading to thermal expansion and localized increases in pressure depending on the target's dielectric parameters via the thermoacoustic effect. This pressure increase, referred to as the initial pressure distribution, relaxes as broadband ultrasound waves that are then measured on the boundary of the target. A thermoacoustic image, i.e. an estimate of the initial pressure distribution, is then reconstructed from the measured ultrasound waves. Thus, TAT combines the electromagnetic contrast arising from interactions of microwaves in of biological tissues with the high resolution of ultrasound imaging.

Thermoacoustic tomography is qualitative by nature and does not allow for quantitative analysis of tissue properties such as various physiological processes. TAT can, however, be extended to its quantitative counterpart (quantitative thermoacoustic tomography, QTAT), where the aim is to estimate the dielectric parameters of the imaged target [9–11]. Due to the changes observed in the dielectric parameters in pathologies, such as perfusion changes in ischemic or hemorrhagic stroke [12,13], and various tumors [14–16], QTAT has significant potential as a diagnostic tool for these conditions, as well as for imaging other physiological processes.

The inverse problem of QTAT can be approached in two stages. First, the initial pressure distribution is estimated from the measured ultrasound waves by solving the acoustic inverse problem. Then, in the electrical inverse problem, the dielectric parameters are estimated from the initial pressure distribution. The acoustic inverse problem, that is similar to the inverse problem in photoacoustic tomography, has been widely studied, and various approaches for its solution have been considered. These approaches can be broadly categorized into analytical approaches, approaches utilizing a numerical approximation of the forward model such as time-reversal, least-squares approaches and the Bayesian approach, and deep learning-based techniques, see e.g. [17–20] and the references therein.

The previous research on the electrical inverse problem of QTAT has mostly focused on its theoretical foundations. Uniqueness and stability results for estimating conductivity in the electrical inverse problem using the vectorial Maxwell's equations and the Helmholtz equation were given in [21] and a reconstruction approach using the Helmholtz equation was presented in [22]. Furthermore, uniqueness results for estimating both conductivity and permittivity in the electrical inverse problem for the vectorial Maxwell's equation were given in [10] and uniqueness and stability results for a system of semilinear Helmholtz equations were presented in [23]. Notably, in [10] it was shown that multiple incident electric fields inducing sufficiently differ-

ent initial pressure distributions are required for to obtain a unique solution to the electrical inverse problem. For numerical implementations, results for estimating the conductivity using the Helmholtz and Maxwell's equations were presented in [21], and estimating the Gruneisen parameter, susceptibility, and conductivity using the system of semilinear Helmholtz equations were presented in [23]. Finally, numerical results for estimating the conductivity and permittivity using the Maxwell's equations were presented in [11].

Only few studies have considered the full QTAT inverse problem of estimating the dielectric parameters from ultrasound waves. A model taking into account slowly varying electromagnetic sources and a formal approach for the inverse problem was presented in [9], and the uniqueness and stability of reconstructing small conductivity inclusions was studied in [24].

In this work, we study simultaneous estimation of electrical conductivity and permittivity in the inverse problem of QTAT. The problem is solved in two stages by first solving the acoustic and then the electrical inverse problem. The forward models are based on the Maxwell's equations and the acoustic wave equation, that are numerically approximated using the finite element method (FEM) and the pseudospectral k-space method, respectively. The approach is evaluated with numerical simulations using a varying number of electromagnetic sources, and full and limited-view ultrasound sensor geometries.

The remainder of this paper is organised as follows. Modelling of electromagnetic and acoustic wave propagation is presented in Sec. 2. The acoustic and electrical inverse problems are described in Sec. 3, and numerical simulations are presented in Sec. 4. Finally, the results are discussed and conclusions are given in Sec. 5.

2 Forward problem

In the forward problem of QTAT, the ultrasound waves on the boundary of the target are solved when the dielectric parameters are given. The forward problem is approached in two stages, known as the electrical and acoustic forward problems.

2.1 Electrical forward problem

In the electrical forward problem, the initial pressure distribution is solved when the dielectric parameters of the target and the electromagnetic source are given. Let us consider a domain $\Omega_{\rm el} \subset \mathbb{R}^d$ with a boundary $\partial \Omega$, where d denotes the dimension. We assume non-magnetic, linear, isotropic, and inhomogeneous materials with conductivity $\sigma(r) \geq 0$ and relative permittivity $\epsilon(r) \geq 1$. We further model the electric

fields as time-harmonic [25]

$$\hat{E}(r,t) = \text{Re}(E(r)e^{i\omega t}),\tag{1}$$

where $\hat{E}(r,t)$ is the electric field at time instance t and position r, $\text{Re}(\cdot)$ denotes the real part, $E(r) \in \mathbb{C}^d$ is the complex amplitude, i is the imaginary unit, and ω is the angular frequency.

Propagation of electromagnetic waves is governed by the Maxwell's equations. In this work, we assume that the exterior of $\Omega_{\rm el}$ has constant electrical conductivity $\sigma_{\rm ext} \geq 0$ and relative permittivity $\epsilon_{r,\rm ext} \geq 1$, and use an absorbing type boundary condition. The behavior of the electric fields is then described by the system of equations [25, 26]

$$\begin{cases} \nabla \times \nabla \times E(r) - \gamma^{2}(r)E(r) = 0, & r \in \Omega_{\text{el}} \\ (\nabla \times E(r)) \times \hat{n} + i\kappa \hat{n} \times (E(r) \times \hat{n}) = g(r), & r \in \partial\Omega_{\text{el}}, \end{cases}$$
 (2)

where $\gamma^2(r) = \mu_0(\omega^2 \epsilon_0 \epsilon_r(r) - i\omega\sigma(r))$, ϵ_0 is the permittivity of free space, μ_0 is the permeability of free space, and $\epsilon_r(r)$ is the relative permittivity. Furthermore, $\kappa = \sqrt{\mu_0(\omega^2 \epsilon_0 \epsilon_{r,\text{ext}} - i\omega\sigma_{\text{ext}})}$, and \hat{n} is an outward unit normal. The right-hand side term of the boundary condition describing the electromagnetic source is given by $g(r) = (\nabla \times E_{\text{inc}}(r)) \times \hat{n} + i\kappa \hat{n} \times (E_{\text{inc}}(r) \times \hat{n})$, where E_{inc} is the incident electric field on the boundary $\partial \Omega_{\text{el}}$.

As the electric fields propagate through the domain, they are absorbed, leading to an absorbed energy density [2,9]

$$H(r,t) = \sigma(r)\langle |\hat{E}(r,t)|^2 \rangle, \tag{3}$$

where $\langle \cdot \rangle$ denotes a short-time average over one oscillatory period $T = 2\pi/\omega$ of the electric field. When the absorption of electromagnetic energy is assumed to be instantaneous, i.e. it fulfills the so-called thermal and stress confinement criteria [27], the absorbed energy density can be written as [9,10,23]

$$H(r) = \frac{1}{2}\sigma(r)|E(r)|^2. \tag{4}$$

The initial pressure p_0 is then given in terms of the absorbed energy density as [2,27]

$$p_0(r) = \hat{\Gamma}H(r),\tag{5}$$

where $\hat{\Gamma}$ is the Grüneisen parameter describing the efficiency of the thermoacoustic effect. In this work, the Grüneisen parameter is assumed to be a known constant.

In this work, the solution of (2) is approximated using the FEM with edge elements [11,25,26]. Edge elements are especially suitable for modelling the behavior of electromagnetic fields in complex media due to their ability of incorporating continuity properties and avoiding spurious numerical solutions. The FEM is implemented in MATLAB, utilizing a code package published in [28].

2.2 Acoustic forward problem

In the acoustic forward problem, the ultrasound waves are solved from the initial pressure distribution given by the solution of the electrical forward problem. Propagation of acoustic waves generated by an initial pressure distribution in a domain $\Omega_{\rm ac} \subset \mathbb{R}^d$, in an acoustically homogeneous and non-attenuating medium, is described by the acoustic initial value problem [29, 30]

$$\begin{cases}
\nabla^2 p(r,t) - \frac{1}{v^2} \frac{\partial^2 p(r,t)}{\partial t^2} = 0 \\
p(r,t=0) = p_0(r) \\
\frac{\partial}{\partial t} p(r,t=0) = 0,
\end{cases}$$
(6)

where p(r,t) is the pressure, $p_0(r)$ is the initial pressure, and v is the speed of sound. In this work, the solution of (6) is numerically approximated using the pseudospectral k-space method implemented in the k-Wave toolbox [30].

3 Inverse problem

In the inverse problem of QTAT, the dielectric parameters of the imaged target are estimated from the measured ultrasound waves. The problem is approached in two stages by solving the acoustic and electrical inverse problems.

3.1 Acoustic inverse problem

In the acoustic inverse problem of QTAT, the initial pressure distribution is estimated from the measured ultrasound waves. Let us consider a thermoacoustic measurement system consisting of S ultrasound sensors measuring an ultrasound signal discretized in T time points. The discretized observation model for the acoustic inverse problem is then given by

$$p_t = Kp_0 + e, (7)$$

where $p_t \in \mathbb{R}^{ST}$ is the ultrasound data, $K \in \mathbb{R}^{ST \times L}$ is a discretized linear forward operator describing the acoustic wave equation (6), $p_0 \in \mathbb{R}^L$ is the discretized initial pressure distribution, and $e \in \mathbb{R}^{ST}$ is additive noise.

In the Bayesian framework, the solution of the inverse problem is the posterior distribution $\pi(p_0|p_t)$, that is given by the Bayes' formula [31,32]

$$\pi(p_0|p_t) \propto \pi(p_t|p_0)\pi(p_0),\tag{8}$$

 $\pi(p_t|p_0)$ is the likelihood distribution and $\pi(p_0)$ is the prior distribution of the initial pressure. In the case of mutually independent noise and initial pressure, the likelihood distribution can be written as [31]

$$\pi(p_t|p_0) = \pi_e(p_t - Kp_0), \tag{9}$$

where π_e denotes the probability density of the noise. We model the noise and the initial pressure as Gaussian distributed

$$e \sim \mathcal{N}(\eta_e, \Gamma_e), \quad p_0 \sim \mathcal{N}(\eta_{p_0}, \Gamma_{p_0}),$$

where η_e and η_{p_0} are the expected values, and Γ_e and Γ_{p_0} are the covariance matrices of the noise and initial pressure distributions, respectively.

In the two-stage inverse problem considered in this work, the prior information for the first (acoustic) inverse problem, can be determined by the prior model of the dielectric parameters and the electrical forward model. In this work, the prior model for the acoustic inverse problem is formed for each incident electric field as a Gaussian sample-based approximation [31]

$$\eta_{p_0} = \frac{1}{N} \sum_{n=1}^{N} p_{0,n},\tag{10}$$

$$\Gamma_{p_0} = \frac{1}{N} \sum_{n=1}^{N} p_{0,n} p_{0,n}^{\mathrm{T}} - \eta_{p_0} \eta_{p_0}^{\mathrm{T}}, \tag{11}$$

where $p_{0,n}$ are samples of the initial pressure distribution calculated using the electrical forward model (Eqs. (2), (4)-(5)) from samples drawn from the prior distributions of the dielectric parameters described in Sec. 3.2.

The posterior distribution can then be written as [20,31]

$$\pi(p_0|p_t) \propto \exp\left\{-\frac{1}{2}\|L_e(p_t - Kp_0 - \eta_e)\|_2^2 - \frac{1}{2}\|L_{p_0}(p_0 - \eta_{p_0})\|_2^2\right\},\tag{12}$$

where L_e and L_{p_0} are the Cholesky decompositions of the inverse covariance matrices of the noise and prior distributions $\Gamma_e^{-1} = L_e^{\rm T} L_e$ and $\Gamma_{p_0}^{-1} = L_{p_0}^{\rm T} L_{p_0}$. Due to the linearity of the observation model and Gaussian distributed noise and prior, the posterior distribution is a Gaussian distribution

$$p_0|p_t \sim \mathcal{N}(\eta_{p_0|p_t}, \Gamma_{p_0|p_t}), \tag{13}$$

where the expected value $\eta_{p_0|p_t}$ and covariance matrix $\Gamma_{p_0|p_t}$ are given by

$$\eta_{p_0|p_t} = \Gamma_{p_0|p_t} (K^{\mathrm{T}} \Gamma_e^{-1} (p_t - \eta_e) + \Gamma_{p_0}^{-1} \eta_{p_0}), \tag{14}$$

$$\Gamma_{p_0|p_t} = (\Gamma_{p_0}^{-1} + K^{\mathrm{T}} \Gamma_e^{-1} K)^{-1}. \tag{15}$$

3.2 Electrical inverse problem

In the electrical inverse problem, the dielectric parameters are estimated from the initial pressure distributions that are obtained as the solutions of the acoustic inverse problem. Let us consider initial pressure data induced by M incident electric fields, $P_0 = (p_{0,1}, \ldots, p_{0,M})^{\mathrm{T}} \in \mathbb{R}^{ML}$, where $p_{0,m} = \eta_{p_0|p_t,m}$ is the expected value of the posterior distribution of the initial pressure corresponding the m:th incident electric field given by (14). The discretized observation model for the electrical inverse problem is of the form [11]

$$P_0 = f(x) + \tilde{e},\tag{16}$$

where $x = (\sigma_1, \dots, \sigma_J, \epsilon_{r,1}, \dots, \epsilon_{r,J})^T \in \mathbb{R}^{2J}$ are the discretized dielectric parameters, f is a discretized forward operator Eqs. (2), (4)-(5), and $\tilde{e} \in \mathbb{R}^{ML}$ is additive noise.

Similarly to the acoustic inverse problem, the electrical inverse problem is approached in the Bayesian framework. The posterior distribution is given by [31]

$$\pi(x|P_0) \propto \pi(P_0|x)\pi(x),\tag{17}$$

where $\pi(P_0|x)$ is the likelihood distribution and $\pi(x)$ is the prior distribution of the dielectric parameters. The noise and unknown parameters are modelled as mutually independent and Gaussian distributed

$$\tilde{e} \sim \mathcal{N}(\eta_{\tilde{e}}, \Gamma_{\tilde{e}}), \quad x \sim \mathcal{N}(\eta_x, \Gamma_x),$$

where $\eta_{\tilde{e}}$ and η_x are the expected values, and $\Gamma_{\tilde{e}}$ and Γ_x are the covariance matrices of the noise and dielectric parameter distributions, respectively.

Now, in the case of the two-stage inverse problem, the noise is modeled as zeromean, with a covariance matrix given by the solution of the acoustic inverse problem

$$\eta_{\tilde{e}} = 0, \quad \Gamma_{\tilde{e}} = \operatorname{diag}(\Gamma_{p_0|p_t,1}, \dots \Gamma_{p_0|p_t,M}),$$
(18)

where $\Gamma_{p_0|p_t,m}$ is the covariance matrix of the initial pressure distribution given by (15) corresponding to the m:th incident electric field, and diag(·) denotes a block diagonal matrix. The prior model for the dielectric parameters is chosen as the Gaussian Ornstein-Uhlenbeck distribution [33] with a covariance

$$\Gamma_x = \begin{bmatrix} \tilde{\sigma}_{\sigma}^2 \Pi & 0\\ 0 & \tilde{\sigma}_{\epsilon_x}^2 \Pi, \end{bmatrix}, \tag{19}$$

where $\tilde{\sigma}_{\sigma}$ and $\tilde{\sigma}_{\epsilon_r}$ are the standard deviations of the conductivity and relative permittivity, respectively. Furthermore, Π is defined as

$$\Pi = \exp\left\{-\frac{\|r_i - r_j\|}{\ell}\right\},\tag{20}$$

where r_i and r_j are locations of the elements and ℓ is a characteristic length controlling the spatial correlation.

The posterior distribution can then be written as [11,31]

$$\pi(x|P_0) \propto \exp\left\{-\frac{1}{2}\|L_{\tilde{e}}(P_0 - f(x))\|_2^2 - \frac{1}{2}\|L_x(x - \eta_x)\|_2^2\right\},\tag{21}$$

where L_x and $L_{\tilde{e}}$ are the Cholesky decompositions of the inverse covariance matrices of the prior and noise distributions $\Gamma_x^{-1} = L_x^{\rm T} L_x$ and $\Gamma_{\tilde{e}}^{-1} = L_{\tilde{e}}^{\rm T} L_{\tilde{e}}$, respectively. The posterior distribution (21) could, in principle, be computed using Markov chain Monte Carlo methods. These methods are, however, computationally prohibitive in high-dimensional inverse problems, and thus point estimates are considered. In this work, we compute the maximum a posteriori (MAP) estimate

$$x_{\text{MAP}} = \arg\min_{x} \left\{ \frac{1}{2} \| L_{\tilde{e}}(P_0 - f(x)) \|_2^2 + \frac{1}{2} \| L_x(x - \eta_x) \|_2^2 \right\}.$$
(22)

The MAP estimate is solved using the Gauss-Newton method, where the solution is obtained iteratively as

$$x_{l+1} = x_l + \tilde{\alpha}_l d_l, \tag{23}$$

where $\tilde{\alpha}_l$ is a step length on the l:th iteration. Furthermore, d_l is a search direction given by

$$d_{l} = \left(J_{f(x_{l})}^{T} \Gamma_{\tilde{e}}^{-1} J_{f(x_{l})} + \Gamma_{x}^{-1}\right)^{-1}$$

$$\left(J_{f(x_{l})}^{T} \Gamma_{\tilde{e}}^{-1} (H - f(x_{l})) - \Gamma_{x}^{-1} (x - \eta_{x})\right),$$
(24)

where $J_{f(x_l)} \in \mathbb{R}^{ML \times 2J}$ is the Jacobian matrix of the forward operator f evaluated at the point x_l .

4 Simulations

4.1 Simulation domain

The proposed approach for estimating the dielectric parameters from ultrasound waves in QTAT was studied using 2D numerical simulations. The simulated numerical phantom was defined as a circle with a radius of 5mm. The incident electric

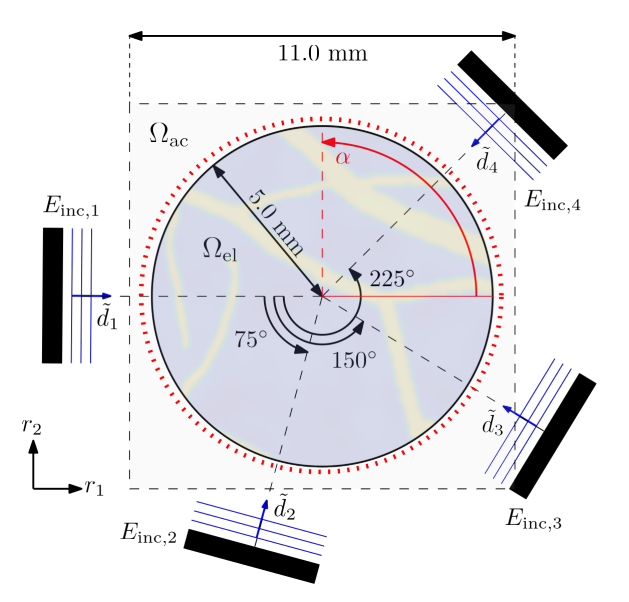


Figure 1: An illustration of the simulation setup. The simulated phantom (circle), and electromagnetic and acoustic domains $\Omega_{\rm ac}$ and $\Omega_{\rm el}$. The incident electric fields $E_{{\rm inc},m}$ are illustrated using black rectangles and propagation directions d_m , where $m=1,\ldots,4$. The ultrasound sensors geometries are shown using red dots and their angular coverage is indicated using the angle α .

fields were modeled as linearly polarized plane waves from four directions around the phantom. Ultrasound sensors were modeled as point-like sensors located on a circular arc at a distance of 0.125 mm from the phantom boundary. The simulated phantom, incident electric fields, and ultrasound sensor geometries are illustrated in Fig. 1.

The electromagnetic simulation domain $\Omega_{\rm el}$ was modeled as the size of the phantom. For ultrasound simulations, a 11.0 \times 11.0 mm square domain $\Omega_{\rm ac}$ centered at the phantom location was considered. The acoustic domain was further extended using a perfectly matched layer (PML) to absorb reflections on the boundary $\partial\Omega_{\rm ac}$.

4.2 Data simulation

Thermoacoustic ultrasound data were simulated using a numerical phantom consisting of blood vessel-like structures shown in Fig.2. Values for the dielectric parameters were chosen in the range of realistic values for biological tissues [34]. The minimum and maximum values of the dielectric parameters were $\sigma_{\min} = 0.14 \, \mathrm{Sm}^{-1}$, $\sigma_{\max} = 1.60 \, \mathrm{Sm}^{-1}$, $\epsilon_{r,\min} = 5.44$, and $\epsilon_{r,\max} = 64.03$. The exterior of the domain was modeled as castor oil with conductivity $\sigma_{\mathrm{ext}} = 10^{-12} \, \mathrm{Sm}^{-1}$ and relative permittivity $\epsilon_{r,\mathrm{ext}} = 4$.

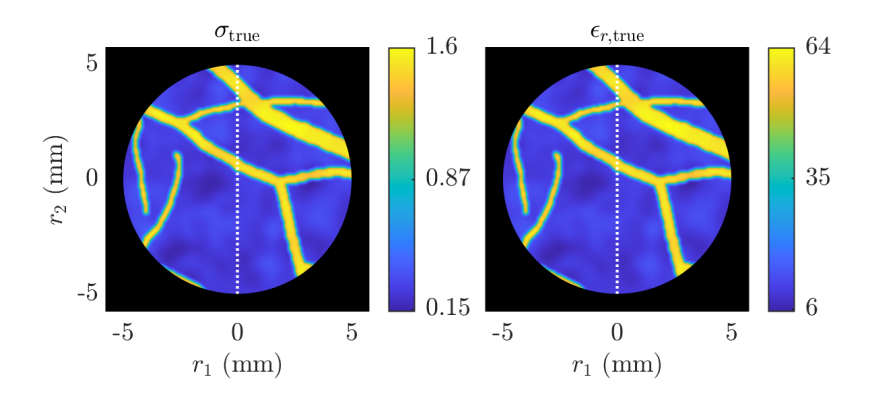


Figure 2: Simulated conductivity σ_{true} (Sm⁻¹, left) and relative permittivity $\epsilon_{r,\text{true}}$ (right). Location of the cross section used for visualising the results is illustrated with a white dotted line.

Table 1: Spatial discretisation used for data simulation and the electrical inverse problem. Number of elements J, number of edges N_e , number of nodes N_n , and average edge length Δh .

Electrical	J	N_e	N_n	$\Delta h (\mu \mathrm{m})$
Simulation	536215	805239	269025	19.5
Inverse	19555	29507	9953	101.9

For the electromagnetic simulations, M=4 incident electric fields were considered. The incident electric fields were modeled as linearly polarized plane waves of the form

$$E_{\text{inc},m}(r) = \tilde{p}_m \exp\left\{-i\kappa \tilde{d}_m \cdot r\right\},\tag{25}$$

where m = 1, ... 4, \tilde{p} is the polarization, $\tilde{d} \in \mathbb{R}^2$ is the propagation direction, and $\|\tilde{d}\| = 1$. The plane waves were polarized perpendicularly to the propagation direction, i.e. $\tilde{d}_m \cdot \tilde{p}_m = 0$. The incident electric field directions are illustrated in Fig. 1. The initial pressures were simulated using the Maxwell's equation (2) and the model (4)–(5) using the FEM as described in Sec. 2.1 in a triangular FE discretization described in Table 1. The Grüneisen parameter was $\hat{\Gamma} = 1$ and the frequency was f = 1 GHz. The simulated initial pressure distributions are illustrated later in Fig. 4.

The initial pressures were then linearly interpolated to a pixel mesh described in Table 2. The ultrasound data was simulated with the acoustic wave equation (6) using the pseudospectral k-space method implemented in the k-Wave toolbox [30] for sensor coverages of $\alpha = 90^{\circ}, 180^{\circ}$, and 360° (Fig. 1). The speed of sound was

Table 2: Spatial and temporal discretisations used for data simulation and the acoustic inverse problem. Number of pixels L, pixel size Δh , PML thickness in pixels, number of time points T, and time step Δt .

	L	$\Delta h \left(\mu \mathrm{m} \right)$	PML	T	$\Delta t (\mathrm{ns})$
Simulation	643^2 123^2	17.1	16	3032	3.4
Inverse		90.0	12	580	18.0

v = 1500 m/s.

After data simulation, Gaussian noise was added to all datasets. The noise was defined as zero-mean and the standard deviation of the noise was chosen as the average of 1% of the maximum simulated ultrasound amplitudes for all incident electric fields $E_{\rm inc}$ using the sensor geometry $\alpha=360^{\circ}$.

4.3 Acoustic inverse problem

For the acoustic inverse problem, the simulated thermoacoustic ultrasound data were linearly interpolated to a coarser temporal discretization described in Table 2 and the initial pressure distributions were estimated using (14)-(15). The initial pressure distributions were estimated for all incident electric fields $E_{\rm inc}$ and angular sensor coverages $\alpha = 90^{\circ}, 180^{\circ}$, and 360°. If the initial pressure included negative values, they were set to zero.

The noise was modelled as Gaussian distributed with zero mean. The standard deviation of the noise was modeled as the average of 1% of the maximum simulated ultrasound amplitudes for all incident electric fields $E_{\rm inc}$ using the sensor geometry $\alpha=360^{\circ}$. The prior distribution (10)-(11) was simulated by drawing N=50000 samples from the Ornstein-Uhlenbeck prior distribution for the dielectric parameters (19)-(20). The expected values $\eta_{p_0|p_t}$, standard deviations $\tilde{\sigma}_{p_0|p_t}$, and blocks of the covariance matrices $\Gamma_{p_0|p_t}$ of the prior distribution for all incident electric fields $E_{\rm inc}$ are visualized in Fig. 3. As can be seen, the expected values and standard deviation exhibit significant differences depending on the direction of the incident electric field. Furthermore, the covariance matrices are highly non-diagonal indicating a degree of spatial correlation.

The estimated expected values $\eta_{p_0|p_t}$ of the initial pressure for angular sensor coverages $\alpha = 90^{\circ}$, 180° , and 360° , and all incident electric fields $E_{\rm inc}$ are shown in Fig. 4. As can be seen, amplitudes of the initial pressure vary significantly depending on the vessel orientation with respect to the incident electric field direction. Furthermore, the effect of the limited-view sensor geometries can be observed as blurring of the phantom structures outside the sensor coverage.

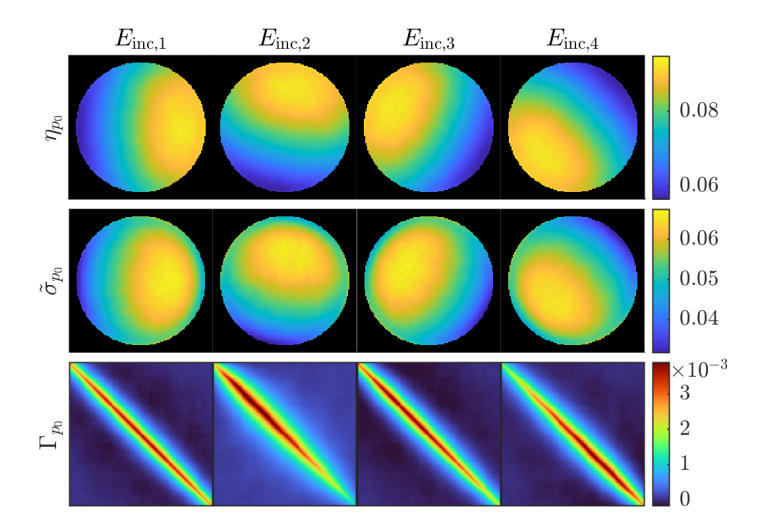


Figure 3: Expected values η_{p_0} (first row), standard deviations $\tilde{\sigma}_{p_0}$ (second row), and blocks of the covariance matrices Γ_{p_0} (third row) of the prior distribution of the initial pressure in the acoustic inverse problem using the incident electric fields $E_{\text{inc},1}$ to $E_{\text{inc},4}$ (columns 1-4). For the covariance matrices, a subsection of the covariance matrix corresponding to the pixels illustrated in Fig. 2 is shown.

4.4 Electrical inverse problem

The data for the electrical inverse problem was given by the expected value of the initial pressure distribution (Eqs. (14)). Furthermore, the noise was given by the covariance of the initial pressure (Eqs. (15) and (18)). The standard deviations $\tilde{\sigma}_{\tilde{e}}$ and blocks of the covariance matrices of the noise $\Gamma_{\tilde{e}}$ for all incident electric fields $E_{\rm inc}$ and sensor geometries $\alpha = 90^{\circ}, 180^{\circ}$, and 360° are illustrated in Fig. 5. As can be seen, the structure of the standard deviation is largely determined by the sensor geometry. The standard deviations are generally largest outside the area covered by the sensor array and vary slightly depending on the direction of the incident electric field. Furthermore, the covariance matrices become increasingly non-diagonal as the sensor coverage decreases.

The expected value and standard deviation of the Ornstein-Uhlenbeck prior distribution (19)–(20) for the dielectric parameters were chosen as $\eta_{\sigma} = \frac{1}{2}(\sigma_{\text{max}} + \sigma_{\text{min}})$, $\eta_{\epsilon_r} = \frac{1}{2}(\epsilon_{r,\text{max}} + \epsilon_{r,\text{min}})$, $\tilde{\sigma}_{\sigma} = \frac{1}{3}(\sigma_{\text{max}} - \sigma_{\text{min}})$, and $\tilde{\sigma}_{\epsilon_r} = \frac{1}{3}(\epsilon_{r,\text{max}} - \epsilon_{r,\text{min}})$, where the subscripts max and min refer to the maximum and minimum values of the phantom. The characteristic length was $\ell = 1$ mm.

The electrical conductivity σ and relative permittivity ϵ_r were estimated by minimizing (22). The dielectric parameters were estimated using data from one to four incident electric fields $E_{\rm inc}$ and angular sensor coverages of $\alpha = 90^{\circ}, 180^{\circ}$, and 360°.

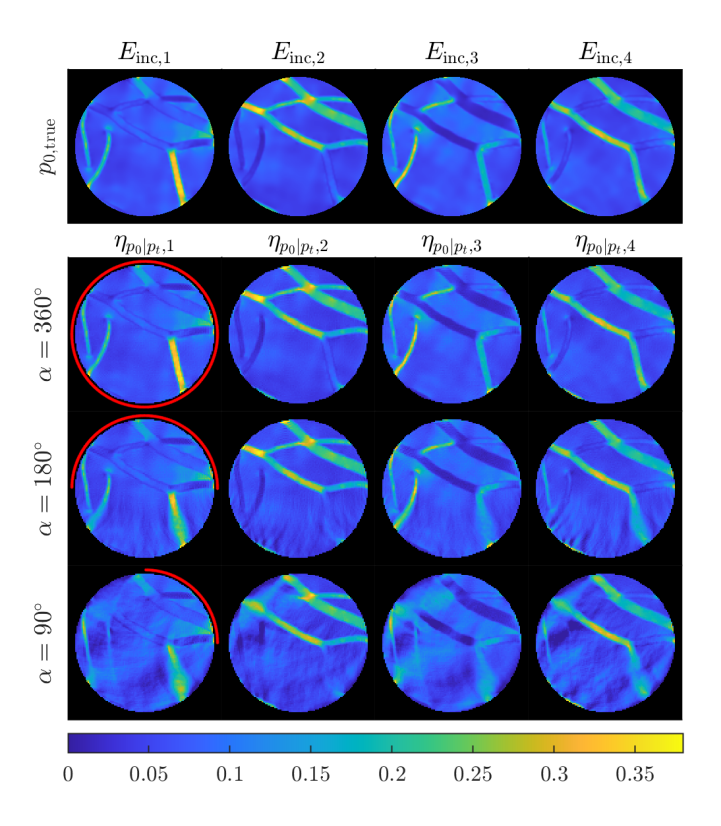


Figure 4: Simulated (true) initial pressure p_0 , (first row) and estimated initial pressures $\eta_{p_0|p_t}$ (rows 2-4) for all incident electric fields $E_{\rm inc}$ (columns 1-4) and sensor geometries $\alpha=90^\circ,180^\circ$, and 360°. The sensor geometries are illustrated using red arcs.

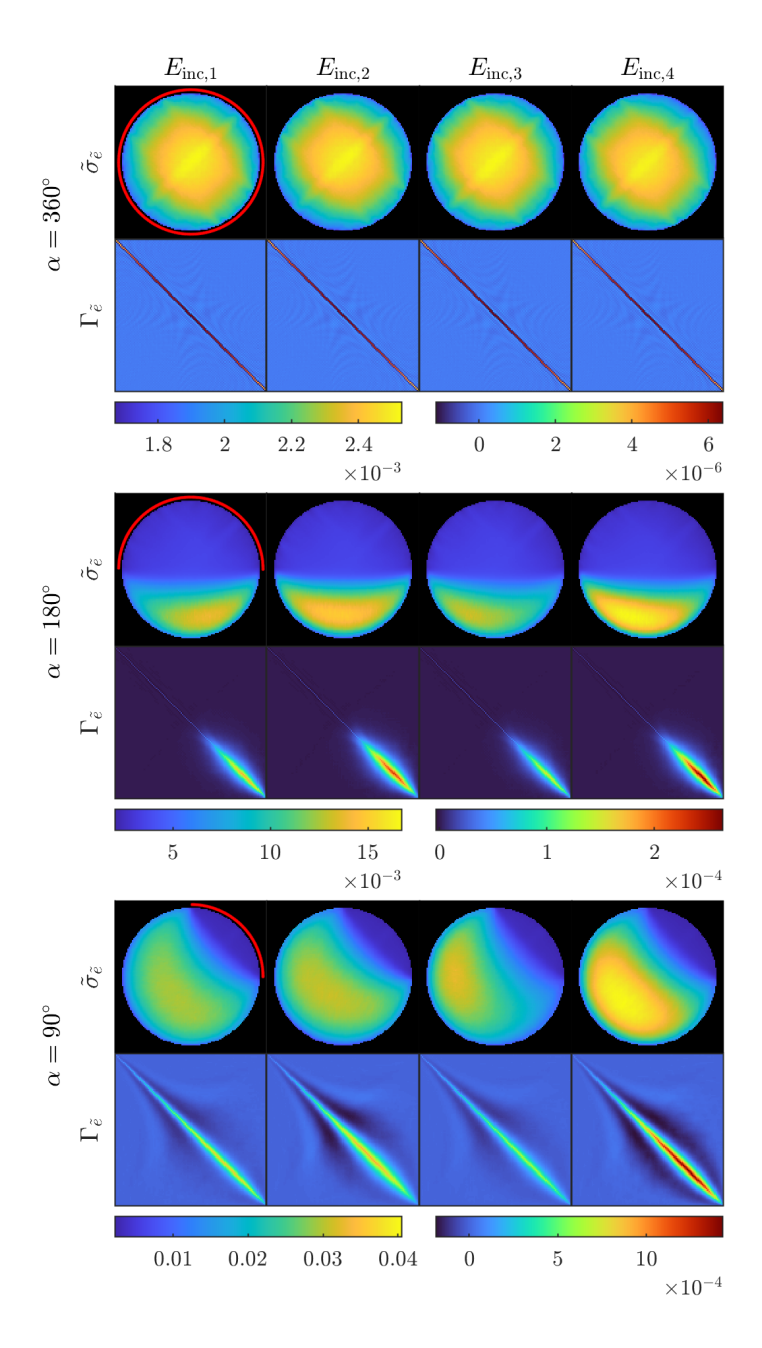


Figure 5: Standard deviations $\sigma_{\tilde{e}}$ and blocks of the covariance matrices $\Gamma_{\tilde{e}}$ of the noise for the electrical inverse problem for incident electric fields $E_{\rm inc,1}$ to $E_{\rm inc,4}$ (columns 1-4), and sensor geometries $\alpha=90^\circ,180^\circ$, and 360° (rows 1-6). For the covariance matrices, a subsection of the covariance matrix corresponding to the pixels indicated in Fig. 2 is shown. The sensor geometries are illustrated using red arcs.

The minimization problem (22) was solved with the Gauss-Newton method (23). The minimization problem was equipped with constraints $\sigma \geq 0$ and $\epsilon_r \geq 1$, and the initial guess of the minimization algorithm was set to the expected value of the prior distribution. The minimization problem was iterated for a minimum of 10 iterations. The iterations were stopped if the objective function value increased for three consecutive iterations or maximum number of 25 iterations was reached.

The MAP estimates of the conductivity σ_{MAP} and relative permittivity $\epsilon_{r,\text{MAP}}$ for one to four incident electric field E_{inc} and sensor geometries $\alpha = 90^{\circ}, 180^{\circ}$, and 360° are shown in Fig. 6. Corresponding cross-sectional line plots are shown in Fig. 7. As can be seen, the number of incident electric fields has a significant effect on the accuracy of the estimated parameters. In the case of one incident electric field, the estimates are highly inaccurate for all sensor geometries. In the case of two incident electric fields, relatively accurate estimates can be obtained when using the full view sensor geometry. Furthermore, in the case of three and four incident electric fields, the estimates are close to the true values for the full-view sensor geometry. Furthermore, the effect of the limited-view ultrasound sensor geometries can be observed as errors and artifacts in the areas where the limited-view artifacts are seen in the estimated initial pressures (Fig. 4).

5 Discussion and conclusions

In this work, an approach for estimating dielectric parameters from thermoacoustic ultrasound waves was presented. The inverse problem was approached in the Bayesian framework and was solved in two stages. The approach was studied using varying number of incident electric fields, and both full-view and limited-view ultrasound sensor geometries.

The results of this study highlight two major factors influencing the accuracy of the estimated dielectric parameters in QTAT. First, the number of electromagnetic pulses has a significant effect on the estimated dielectric parameters. In previous works on QTAT it has been shown that multiple electromagnetic pulses inducing sufficiently different initial pressures are required for obtaining a unique solution to the electrical inverse problem [10,11]. In this work, we observed that three electromagnetic pulses from different directions around the target were sufficient to achieve accurate estimates, whereas two pulses resulted in reasonably accurate estimates when using a full-view ultrasound sensor geometry. The optimal number of pulses is, however, likely to depend on factors such as the chosen field directions, pulse frequency, polarization, and the properties of the imaged target. Second, the geometry of the ultrasound sensor array has a significant effect on the reconstruction quality. While accurate estimates can be achieved within the region enclosed by the sensors, esti-

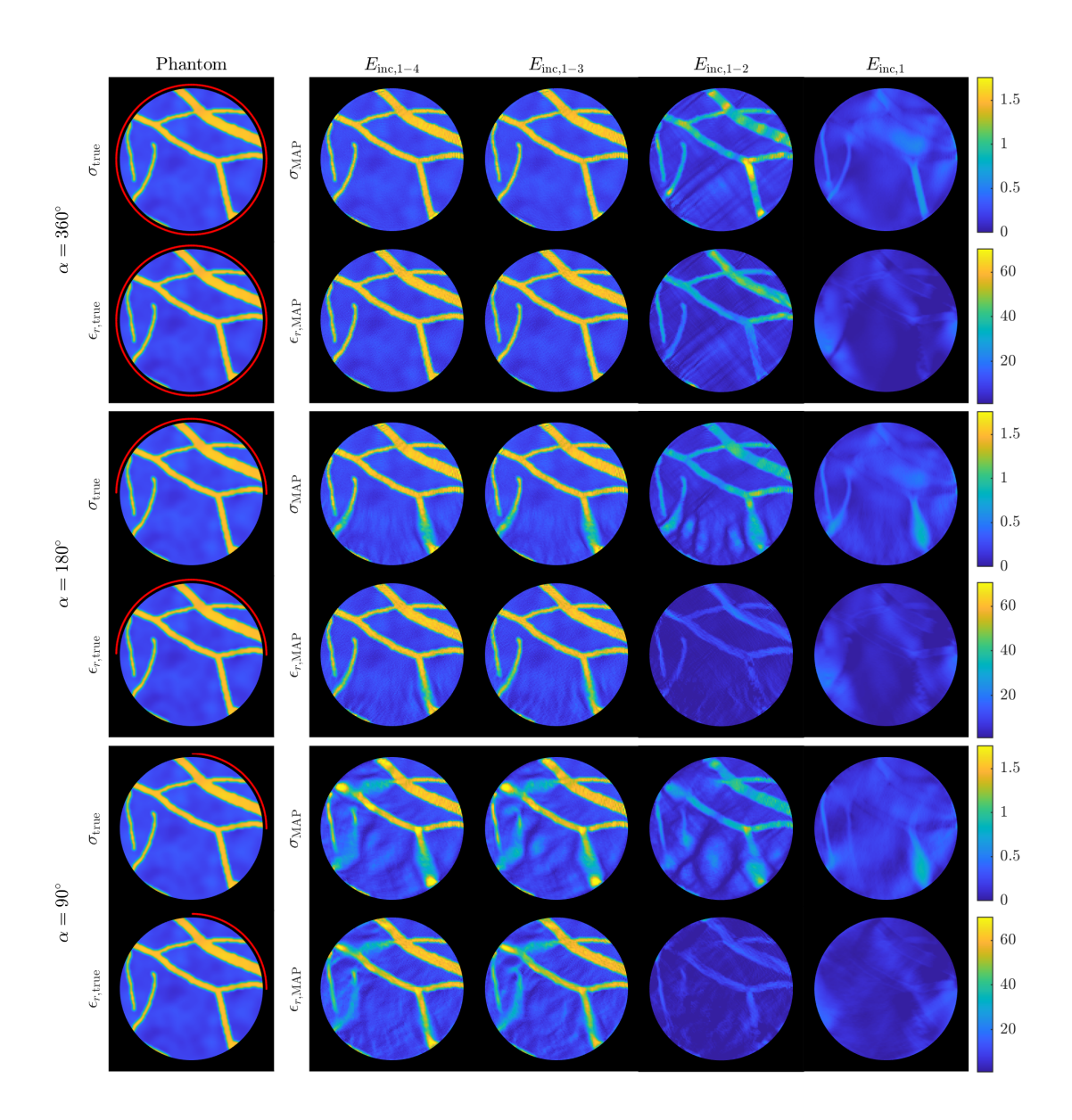


Figure 6: MAP estimates for conductivity σ_{MAP} (rows 1, 3, and 5) and relative permittivity $\epsilon_{r,\text{MAP}}$ (rows 2, 4, and 6) for one to four incident electric fields E_{inc} (columns 2-5) and sensor geometries $\alpha = 360^{\circ}, 180^{\circ}$, and 90° (rows 1-2, 3-4, and 5-6). The true dielectric parameters σ_{true} and $\epsilon_{r,\text{true}}$ are shown in the first column. The sensor geometries are shown using red arcs.

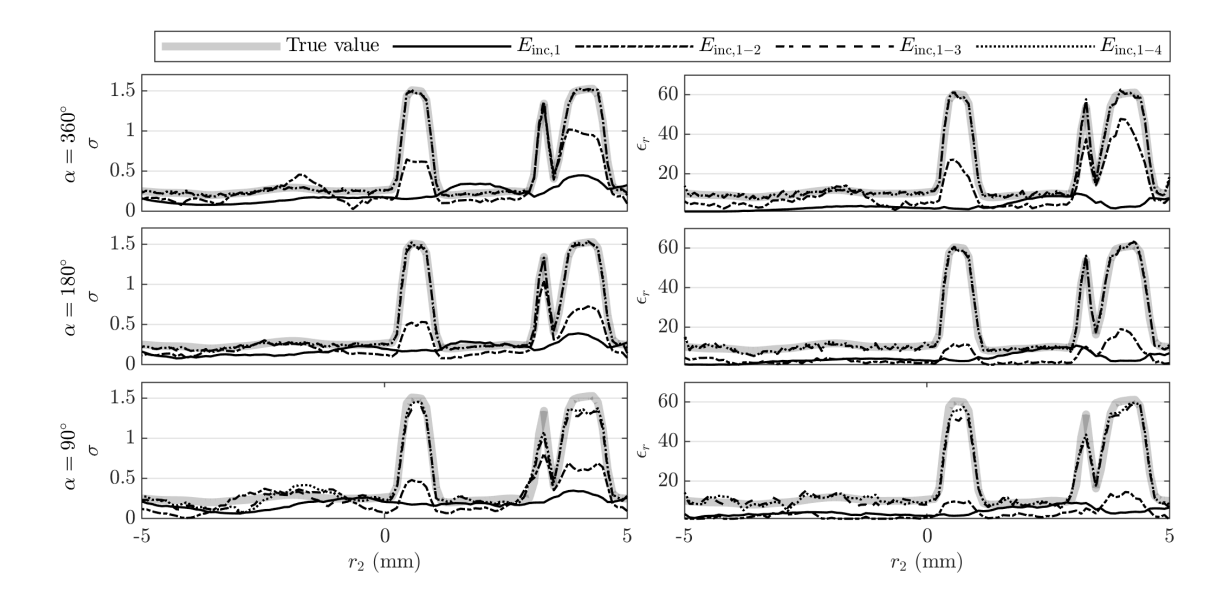


Figure 7: Cross sections of the MAP estimates for conductivity σ_{MAP} (first column) and relative permittivity $\epsilon_{r,\text{MAP}}$ (second column) using one to four incident electric fields E_{inc} for sensor geometries $\alpha = 90^{\circ}, 180^{\circ}$, and 360° (rows 1-3). The parameters are visualized on a vertical cross section through the domain illustrated in Fig. 2.

mates suffer from artifacts further away from the sensor array. These errors originate from limited view artifacts present in the solution of the acoustic problem that can be further exacerbated when using sparsely positioned sensor arrays.

To move towards realistic measurement systems, ultrasound sensors with finite size and bandwidth should be considered. Moreover, the use of plane wave electric fields and the assumption of instantaneous electromagnetic energy absorption may not accurately represent practical systems, particularly when the target is positioned near a realistic waveguide or antenna source. Finally, since propagation of acoustic and electromagnetic waves are inherently three dimensional, the proposed approach should be extended to a three dimensional setting where realistic ultrasound sensors and more realistic electromagnetic models, boundary conditions, and electromagnetic sources can be taken into account.

Biological tissues generally exhibit frequency-dependent dielectric properties, and the propagation of electromagnetic waves in a complex medium can change significantly with the frequency of the applied electric field. In this work, the inverse problem was studied using an electric field frequency of 1 GHz, which offers a favorable trade-off between penetration depth and electromagnetic contrast. To gain additional insight into the proposed method, future studies should account for the frequency-dependent dielectric parameters and investigate the problem using multiple

electric field frequencies.

Overall, it can be concluded that the dielectric parameters can be accurately estimated using the proposed approach, and relatively accurate estimates can be obtained even in severely limited-view ultrasound sensor geometries as long as sufficiently many electromagnetic pulses are used.

Acknowledgments

The authors would like to thank Professor Amelie Litman and Timo Lähivaara for insightful discussions and suggestions.

References

- [1] J. C. Lin, "Microwave thermoacoustic tomographic (mtt) imaging," *Physics in Medicine & Biology*, vol. 66, no. 10, p. 10TR02, 2021.
- [2] C. Li and L. V. Wang, "Photoacoustic tomography and sensing in biomedicine," *Physics in Medicine & Biology*, vol. 54, pp. R59–R97, 2009.
- [3] D. Fallon, L. Yan, G. W. Hanson, and S. K. Patch, "Rf testbed for thermoacoustic tomography," *Review of Scientific Instruments*, vol. 80, no. 6, p. 064301, 2009.
- [4] S. K. Patch, "Towards quantitative whole organ thermoacoustics with a clinical array plus one very low frequency channel applied to prostate cancer imaging," *IEEE Transactions on Ultrasonics Ferroelectrics and Frequency Control*, vol. 63, no. 2, pp. 245–255, 2016.
- [5] S. Kellnberger, A. Hajiaboli, D. Razansky, and V. Ntziachristos, "Near-field thermoacoustic tomography of small animals," *Physics in Medicine & Biology*, vol. 56, no. 11, pp. 3433–3444, 2011.
- [6] O. Ogunlade and P. Beard, "Exogenous contrast agents for thermoacoustic imaging: An investigation into the underlying sources of contrast," *Medical Physics*, vol. 42, no. 1, pp. 170–180, 2015.
- [7] C. Li, M. Pramanik, G. Ku, and L. V. Wang, "Image distortion in thermoacoustic tomography caused by microwave diffraction," *Physical Review E*, vol. 77, p. 031923, 2008.

- [8] R. A. Kruger, K. K. Kopecky, A. M. Aisen, D. R. Reinecke, G. A. Kruger, and W. L. K. Jr, "Thermoacoustic CT with radio waves: A medical imaging paradigm," *Radiology*, vol. 211, no. 1, pp. 275–278, 1999.
- [9] H. Akhouayri, M. Bergounioux, A. Da Silva, P. Elbau, A. Litman, and L. Mindrinos, "Quantitative thermoacoustic tomography with microwaves sources," *Journal of Inverse and Ill-posed Problems*, vol. 25, no. 6, pp. 703–717, 2017.
- [10] G. Bal and T. Zhou, "Hybrid inverse problems for a system of Maxwell's equations," *Inverse Problems*, vol. 30, p. 055013, 2014.
- [11] T. Sahlström, T. Lähivaara, and T. Tarvainen, "Simultaneous estimation of electrical conductivity and permittivity in quantitative thermoacoustic tomography," *Inverse Problems*, vol. 41, no. 3, p. 035015, 2025.
- [12] S. Y. Semenov, S. R. Svenson, and G. P. Tatsis, "Microwave spectroscopy of myocardial ischemia and infarction. 1. experimental study," *Annals of Biomedical Engineering*, vol. 28, pp. 48–54, 2000.
- [13] S. Y. Semenov, R. H. Svenson, V. G. Posukh, A. G. Nazarov, Y. E. Sizov, A. E. Bulyshev, A. E. Souvorov, W. Chen, J. Kasell, and G. P. Tasis, "Microwave spectroscopy of myocardial ischemia and infarction. 1. experimental studydielectrical spectroscopy of canine myocardium during acute ischemia and hypoxia at frequency spectrum from 100 khz to 6 ghz," *IEEE Transactions on Medical Imaging*, vol. 21, no. 6, pp. 703–707, 2002.
- [14] Y. Cheng and M. Fu, "Dielectric properties for non-invasive detection of normal, benign, and malignant breast tissues using microwave theories," *Thorasic Cancer*, vol. 9, no. 4, pp. 459–465, 2018.
- [15] M. Hussein, F. Awwad, D. Jithin, H. El Hasasna, K. Athamneh, and R. Iratni, "Breast cancer cells exhibits specific dielectric signature in vitro using the openended coaxial probe technique from 200 mhz to 13.6 ghz," *Scientific Reports*, vol. 9, no. 1, p. 4681, 2019.
- [16] E. G. Fernández-Aranzamendi, P. E. Castillo-Aranibar, E. G. S. R. Castillo, B. S. Oller, L. Ventura-Zaa, G. Eguiluz-Rodrigues, V. Gonzáles-Posadas, and D. Segovia-Vargas, "Dielectric characterization of ex-vivo breast tissues: Differentiation of tumor types through permittivity measurements," *Cancers*, vol. 16, no. 4, p. 793, 2024.

- [17] J. Poudel, Y. Lou, and M. Anastasio, "A survey of computational frameworks for solving the acoustic inverse problem in three-dimensional photoacoustic computed tomography," *Physics in Medicine & Biology*, vol. 64, no. 14, p. 14TR01, 2019.
- [18] P. Kuchment and L. Kunyansky, *Mathematics of photoacoustic and thermoacoustic tomography*. Springer New York, 2011, ch. 19, pp. 817–865.
- [19] A. Hauptmann and B. Cox, "Deep learning in photoacoustic tomography: current approaches and future directions," *Journal of Biomedical Optics*, vol. 25, p. 112903, 2020.
- [20] J. Tick, A. Pulkkinen, and T. Tarvainen, "Image reconstruction with uncertainty quantification in photoacoustic tomography," The Journal of the Acoustical Society of America, vol. 139, pp. 1951–1961, 2016.
- [21] G. Bal, K. Ren, G. Uhlmann, and T. Zhou, "Quantitative thermo-acoustics and related problems," *Inverse Problems*, vol. 27, no. 5, p. 055007, 2011.
- [22] H. Ammari, J. Garnier, W. Jiang, and L. H. Nguyen, "Quantitative thermoacoustic imaging: An exact reconstruction formula," *Journal of Differential Equations*, vol. 254, no. 3, pp. 1375–1395, 2013.
- [23] K. Ren and N. Soedjak, "Recovering coefficients in a system of semilinear Helmholtz equations from internal data," *Inverse Problems*, vol. 40, no. 4, p. 045023, 2024.
- [24] H. A. Jebawy and A. E. Badia, "Direct algorithm for reconstructing small absorbers in thermoacoustic tomography problem from a single data," *Inverse Problems*, vol. 36, no. 6, p. 065010, 2020.
- [25] P. Monk, Finite Element Methods for Maxwell's Equations. United Kingdom: Claredon Press, 2003.
- [26] M. Bonazolli, "Efficient high order and domain decomposition methods for the time-harmonic maxwell's equations," Ph.D. dissertation, Université Côte D'Azur, 2017.
- [27] L. V. Wang, Photoacoustic Imaging and Spectroscopy. CRC Press, 2009.
- [28] L. Chen, "iFEM: an integrated finite element methods package in MATLAB," Tech. Rep., 2009. [Online]. Available: https://github.com/lyc102/ifem

- [29] B. T. Cox and P. C. Beard, "Fast calculation of pulsed photoacoustic fields in fluids using k-space methods," *The Journal of the Acoustical Society of America*, vol. 117, no. 6, pp. 3616–3627, 2005.
- [30] B. E. Treeby and B. T. Cox, "k-wave: Matlab toolbox for the simulation and reconstruction of photoacoustic wave-fields," *Journal of Biomedical Optics*, vol. 15, no. 2, p. 021314, 2010.
- [31] J. Kaipio and E. Somersalo, Statistical and Computational Inverse problems. Springer-Verlag, 2006.
- [32] D. Calvetti and E. Somersalo, *Bayesian Scientific Computing*. Springer-Verlag, 2024.
- [33] C. E. Rasmussen and C. K. I. Williams, Gaussian Processes for Machine Learning. MIT Press, 2006.
- [34] C. Gabriel, "Compilation of the dielectric properties of body tissues at rf and microwave frequencies," Defence technical information center, 1996.